V European Conference on Computational Fluid Dynamics
ECCOMAS CFD 2010
J. C. F. Pereira and A. Sequeira (Eds)
Lisbon, Portugal,14–17 June 2010

NUMERICAL SIMULATION OF UNSTEADY DUSTY GAS FLOW THROUGH THE MOVING AND STATIONARY CASCADES OF AIRFOILS

D.A. Romanyuk and Yu.M. Tsirkunov

Baltic State Technical University, Faculty of Aerospace Engineering
1st Krasnoarmeiskaya str. 1, 190005 Saint Petersburg, Russia
e-mail: tsrknv@bstu.spb.su

Key words: Cascades of Airfoils, Two-Phase Gas–Particle Flow, Unsteady Flow, Navier–Stokes Equations, Distribution of Particles in Size, Computational Simulation

Abstract. *Dusty gas through a set of two cascades of airfoils (blades) is studied numerically. The first cascade (rotor) moves and the second one (stator) is immovable. Such a flow can be considered, in some sense, as a flow in an inlet stage of a turbomachine, for example, for an inlet compressor of an aircraft turbojet engine. The particle concentration is assumed to be very low, so that a two-phase gas–particle flow can be considered as dilute. The reverse effect of the particle phase on the carrier gas flow and the inter-particle collisions are negligible. Time-dependent two-dimensional gas flow is described by the complete Navier–Stokes equations. The particles are assumed to be solid spheres, monosized or distributed Log-normally in size. The particle drag force, the transverse Magnus force, and the damping torque are taken into account in the model of gas-particle interaction. Impact interaction of particles with blades is considered as frictional and not completely elastic. Flow fields of the carrier gas and flow patterns of the particle phase are obtained and discussed.*

1 INTRODUCTION

Flow through cascades of airfoils occurs in aircraft turbojet engines and other axial turbomachines. In practice, a working gas flowing through a machine channel often contains suspended solid particles or liquid droplets. The presence of a dispersed phase in the flow results in some new effects which more often than not, are undesirable. Specifically, it causes the erosion of blades due to multiple impacts of particles or droplets with them and the additional momentum and energy losses [1]. In this case, the protection of blades from erosion becomes one of the key problems. The most vulnerable to particles' "attack" is an inlet stage of a turbomachine. For prediction of areas on blade surfaces which are exposed to the strongest erosive effect, it is necessary to have a clear insight into characteristic features of the particles' behaviour in the flow. Actual flow in a turbomachine channel is, strictly speaking, three-dimensional. The 3D-effects are particularly essential near the axis and the channel walls. However, some important flow features in the inlet stage and in the sequential rims can be studied with the use of 2D-flow model. Such an approach turned out very fruitful and brought the well-known 2D-theory

of cascade flow into being (e.g., [2]). This theory deals with steady-state dust-free gas flows. Steady-state flow of gas-particle mixture through an immovable cascade was analyzed by Hussein and Tabakoff [3]. Steady-state gas-particle flow model was used in [4] to study the flow in a single rotating cascade.

In the present study the behaviour of solid particles in the time-dependent high-speed subsonic 2D-flow in a set of two, moving and stationary, cascades of blades is simulated numerically and the results are discussed and analyzed. The particle mass load is assumed to be very low, so that the inter-particle collisions and the effect of the dispersed phase on the carrier gas flow can be neglected. In this case, the problem of two-phase flow simulation is reduced to the sequential solving of two problems: (i) computation of the carrier gas flow field, and (ii) calculation of the particles' motion in this flow field. The input data in computations (flow properties, speed of the moving cascade, airfoil sizes, etc.) are chosen to be close to those in the flow through an axial compressor of an aircraft turbojet engine. The main aim of this study is to understand how such actual effect as the particles' distribution in size influences the particle phase flow structure in a complex vortex flow of a dusty gas through the inlet system "rotor-stator" of a turbojet engine.

2 FORMULATION OF THE PROBLEM

2.1 Schematic of flow

We consider a two-phase gas–particle flow through a set of two cascades, the first of which moves with the constant velocity V_r and the second one is stationary (see Fig. 1). Both cascades have the same step s (distance between airfoils along a cascade). Airfoils of the first cascade are set at an angle β with respect to the undisturbed flow direction. For visualization of the particle-phase flow in computational simulation, particles from a cloud of finite width h equal to the airfoil chord l are considered.

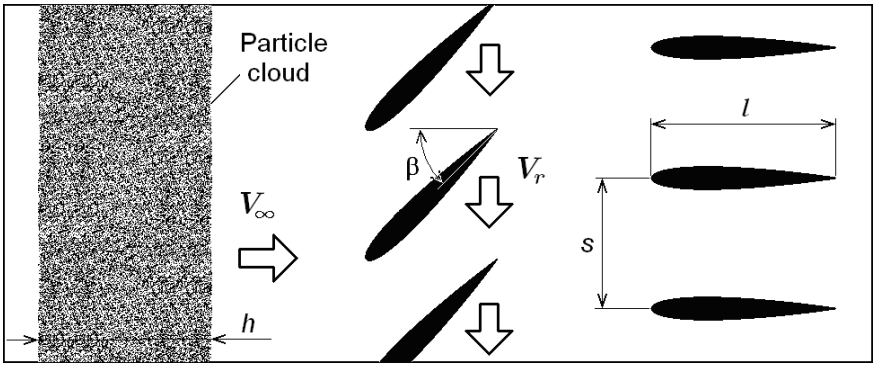

Figure 1: Schematic of arrangement of the two cascades in an undisturbed flow.

A two-phase flow is considered as dilute and one-way coupled. Estimates for the particle concentration when this model is valid have been obtained in [5]. They show that the upper

bound of the concentration depends on the particle size, all other parameters being fixed. Motion of particles is governed by the gas–particle interaction and the particle–blade collisions. Particles being more inertial compared with the carrier gas do not follow streamlines, they can collide with blades and rebound from them. Trajectories of rebounded (reflected) particles can intersect with each other and with the ones of incident particles. Calculations of a large number of particles allow to understand the specific features of particles' behaviour in the flow. Because the gas–particle flow considered in the present study is time-dependent, instant flow patterns of the carrier gas and the particle phase are given and discussed below.

2.2 Modelling of the carrier gas flow

The classical theory of cascades is based on the model of inviscid gas. Preliminary computational simulation of a high-speed subsonic gas flow through the "rotor–stator" set of cascades was performed on the basis of the Euler equations and the complete Navier–Stokes equations. The same grid was used in the computation domain in both cases. Comparison of the results showed that the effects associated with gas viscosity (development of boundary layers on airfoils and vortex wakes behind them) played an important role in forming the flow structure. The Reynolds number $Re_\infty = \rho_\infty V_\infty l/\mu_\infty$, where l is the chord of an airfoil, is approximately equal to $1.4 \cdot 10^6$ in our problem, hence, the flow is actually turbulent, and a commonly accepted approach in this case requires the use of the Reynolds averaged Navier–Stokes equations instead of the Navier–Stokes equations by themselves. However, we share this judgment only in part. The matter is that the large-scale vortex flow structure, which is of greatest important in many applications, can be obtained very often without a fine resolution of small turbulent eddies, and sometimes even without the boundary layer effects. Some evidence for this contention is given in Appendix where the vortex structure of separated flow behind a cylinder obtained by computational simulation with the use of three different flow models is shown and briefly discussed. The Navier–Stokes equations for time-depended compressible 2D-flow can be written in the Cartesian coordinates (x, y) in the following compact form [6]:

$$\frac{\partial \mathbf{Q}}{\partial t} + \frac{\partial \mathbf{F}_x}{\partial x} + \frac{\partial \mathbf{F}_y}{\partial y} = \frac{\partial \mathbf{G}_x}{\partial x} + \frac{\partial \mathbf{G}_y}{\partial y}, \tag{1}$$

where vectors $\mathbf{Q}$, $\mathbf{F}_x$, $\mathbf{F}_y$, $\mathbf{G}_x$, and $\mathbf{G}_y$ are defined as follows:

$$\mathbf{Q} = \begin{pmatrix} \rho \\ \rho u \\ \rho v \\ \rho e \end{pmatrix}, \quad \mathbf{F}_x = \begin{pmatrix} \rho u \\ \rho u^2 + p \\ \rho uv \\ (\rho e + p)u \end{pmatrix}, \quad \mathbf{F}_y = \begin{pmatrix} \rho v \\ \rho uv \\ \rho v^2 + p \\ (\rho e + p)v \end{pmatrix}, \tag{2}$$

$$\mathbf{G}_x = \begin{pmatrix} 0 \\ \tau_{xx} \\ \tau_{yx} \\ u\tau_{xx} + v\tau_{yx} - q_x \end{pmatrix}, \quad \mathbf{G}_y = \begin{pmatrix} 0 \\ \tau_{xy} \\ \tau_{yy} \\ u\tau_{xy} + v\tau_{yy} - q_y \end{pmatrix}.$$

Here

$$\tau_{xx} = \frac{2}{3}\mu\left(2\frac{\partial u}{\partial x} - \frac{\partial v}{\partial y}\right), \quad \tau_{yy} = \frac{2}{3}\mu\left(2\frac{\partial v}{\partial y} - \frac{\partial u}{\partial x}\right), \quad \tau_{xy} = \tau_{yx} = \mu\left(\frac{\partial u}{\partial y} + \frac{\partial v}{\partial x}\right), \qquad (3)$$

$$q_x = -k\frac{\partial T}{\partial x}, \quad q_y = -k\frac{\partial T}{\partial y}, \qquad p = \rho\Re T, \qquad e = c_V T + (1/2)(u^2 + v^2).$$

In the above equations, t is the time; ρ, p, e, T, μ, k are the gas density, the pressure, the specific total energy, the temperature, the viscosity, and the thermal conductivity, respectively; u and v are the x- and y-components of the velocity vector; $\Re$ is the specific gas constant, c_V is the specific heat at constant volume. We use the following relations for μ and k:

$$\mu = \mu_0\left(\frac{T}{T_0}\right)^{3/2}\frac{T_0 + S_0}{T + S_0}, \qquad k = c_p\mu/\mathrm{Pr}. \qquad (4)$$

Here the first relation is the Sutherlend formula, c_p is the specific heat at constant pressure, Pr is the Prandtl number.

The system of equations (1)–(4) is closed. In the present study, it is solved numerically. The boundary conditions with application to the computation domain will be described in Subsection 3.1.

2.3 Modelling of the particle phase flow

The Lagrangian approach is used for modelling the particles' motion. The motion of a particle is described by the momentum and angular momentum equations which are added by the kinematic relation between the particle position vector $\mathbf{r}_\mathrm{p}$ and the velocity vector $\mathbf{v}_\mathrm{p}$

$$m_\mathrm{p}\frac{d\mathbf{v}_\mathrm{p}}{dt} = \mathbf{f}_\mathrm{D} + \mathbf{f}_\mathrm{M}, \qquad J_\mathrm{p}\frac{d\boldsymbol{\omega}_\mathrm{p}}{dt} = \mathbf{l}_\mathrm{p}, \qquad \frac{d\mathbf{r}_\mathrm{p}}{dt} = \mathbf{v}_\mathrm{p}. \qquad (5)$$

Here $m_\mathrm{p} = (4/3)\rho_\mathrm{p}\pi r_\mathrm{p}^3$, $J_\mathrm{p} = (2/5)m_\mathrm{p}r_\mathrm{p}^2$, r_p, and $\boldsymbol{\omega}_\mathrm{p}$ are the particle mass, the moment of inertia, the radius, and the rotational velocity, respectively. We include into the force on a particle the drag force $\mathbf{f}_\mathrm{D}$ and the lift Magnus force $\mathbf{f}_\mathrm{M}$, which dominate all other components in the flow. The Magnus force is developed due to simultaneous translational and rotational motion of a particle, and it can be significant for particles twisted in particle–blade collisions. The damping torque $\mathbf{l}_\mathrm{p}$ acts on a particle if its relative rotational velocity is not zero. We use the conventional relations for calculation of $\mathbf{f}_\mathrm{D}$, $\mathbf{f}_\mathrm{M}$ and $\mathbf{l}_\mathrm{p}$

$$\begin{aligned}
\mathbf{f}_\mathrm{D} &= \frac{1}{2}C_\mathrm{D}\pi r_\mathrm{p}^2\rho|\mathbf{v} - \mathbf{v}_\mathrm{p}|(\mathbf{v} - \mathbf{v}_\mathrm{p}),\\
\mathbf{f}_\mathrm{M} &= \frac{4}{3}C_\omega\pi r_\mathrm{p}^3\rho[(\boldsymbol{\omega} - \boldsymbol{\omega}_\mathrm{p}) \times (\mathbf{v} - \mathbf{v}_\mathrm{p})], \qquad (6)\\
\mathbf{l}_\mathrm{p} &= \frac{1}{2}C_l r_\mathrm{p}^5\rho|\boldsymbol{\omega} - \boldsymbol{\omega}_\mathrm{p}|(\boldsymbol{\omega} - \boldsymbol{\omega}_\mathrm{p}), \qquad \boldsymbol{\omega} = \frac{1}{2}\,\mathrm{curl}\,\mathbf{v}.
\end{aligned}$$

The coefficients $C_{\rm D}$,C_ω and C_l depend on the dimensionless parameters of flow around a particle: the relative Mach and Reynolds numbers, the relative rotational Reynolds number, *etc*. These coefficients are calculated from relations which approximate the results of theoretical and numerical solutions, and experimental data.

For $C_{\rm D}$ we use the Henderson approximate formula [7] for subsonic flow over a particle ($0 < {\rm M_p} < 1$):

$$C_{\rm D}^1({\rm Re_p}, {\rm M_p}, T_{\rm p}/T) =$$

$$= 24\left\{{\rm Re_p} + \sqrt{\frac{\gamma}{2}}{\rm M_p}\left[4.33 + \frac{3.65 - 1.53T_{\rm p}/T}{1 + 0.353T_{\rm p}/T}\exp\left(-0.247\sqrt{\frac{2}{\gamma}}\frac{{\rm Re_p}}{{\rm M_p}}\right)\right]\right\}^{-1}$$

$$+\left[\frac{4.5 + 0.38(0.03{\rm Re_p} + 0.48\sqrt{\rm Re_p})}{1 + 0.03{\rm Re_p} + 0.48\sqrt{\rm Re_p}} + 0.1{\rm M_p^2} + 0.2{\rm M_p^8}\right]\exp\left(-\frac{\rm M_p}{2\sqrt{\rm Re_p}}\right)$$

$$+0.6\sqrt{\frac{\gamma}{2}}{\rm M_p}\left[1 - \exp\left(-\frac{\rm M_p}{\rm Re_p}\right)\right]. \qquad (7)$$

Here ${\rm Re_p} = 2\rho|\mathbf{v} - \mathbf{v}_{\rm p}|r_{\rm p}/\mu$ and ${\rm M_p} = |\mathbf{v} - \mathbf{v}_{\rm p}|/\sqrt{\gamma RT}$ are the relative particle Reynolds and Mach numbers. The dependence of $C_{\rm D}$ on $T_{\rm p}/T$ is very week in the flow under consideration. That is why we ignore this dependence, and take the ratio $T_{\rm p}/T$ equal to unity.

For calculation of C_ω, we use the exact solution by Rubinow and Keller [8] in combination with the approximate formula suggested by Oesterle and Bui Dinh [9]:

$$C_\omega = \begin{cases} 3/4 & 2\gamma_\omega < 0.45, \\ (3/8)\gamma_\omega[0.45 + (2\gamma_\omega - 0.45)\exp(-0.075\gamma_\omega^{0.4}{\rm Re_p^{0.7}})], & 2\gamma_\omega \geq 0.45, \end{cases} \qquad (8)$$

where $\gamma_\omega = \omega_{\rm p} r_{\rm p}/|\mathbf{v} - \mathbf{v}_{\rm p}|$.

The expression for the coefficient C_l is taken in the form [10]:

$$C_l = \frac{C_{l1}}{\sqrt{\rm Re_{p\omega}}} + \frac{C_{l2}}{\rm Re_{p\omega}}, \qquad (9)$$

where ${\rm Re_{p\omega}} = \rho|\boldsymbol{\omega} - \boldsymbol{\omega}_{\rm p}|r_{\rm p}^2/\mu$, and C_{l1} and C_{l2} are given in Table 1.

Table 1: Values of C_{l1} and C_{l2} in relation (9)

${\rm Re_{p\omega}}$	$0-6$	$6-20$	$20-50$	$50-4\times10^4$
C_{l1}	0	5.32	6.44	6.45
C_{l2}	16π	37.2	32.2	32.1

Being involved into the motion by the carrier gas, particles, due to their inertia, do not follow the gas streamlines and can collide with the blades of cascades. We have used the semi-empirical particle–wall collision model [11] for calculating the parameters of a particle just after its rebound. This model is based on the laws of mechanics and the experimental data for the restitution coefficients of the normal ($v_{\rm p}$) and tangential ($u_{\rm p}$) velocities of the center of gravity of a particle (see Fig. 2, left). It is valid at moderate and high particle impact velocities. The final relations for the normal, tangential, and rotational velocities of a particle after its rebound have the form

$$
\begin{aligned}
v_{\rm p2} &= -v_{\rm p1} a_n, \\
u_{\rm p2} &= \begin{cases} u_{\rm p1} a_\tau + \omega_{\rm p1}\, r_{\rm p}(a_\tau - 1), & \beta < \beta_*, \\ u_{\rm p1} a_\tau - \dfrac{2}{7}\,\omega_{\rm p1}\, r_{\rm p}, & \beta \geq \beta_*, \end{cases} \\
\omega_{\rm p2} &= \begin{cases} \dfrac{5}{2}\,\dfrac{u_{\rm p1}}{r_{\rm p}}\,(a_\tau - 1) + \dfrac{5}{2}\,\omega_{\rm p1}\,\left(a_\tau - \dfrac{3}{5}\right), & \beta < \beta_*, \\ -\dfrac{u_{\rm p1}}{r_{\rm p}}\,a_\tau + \dfrac{2}{7}\,\omega_{\rm p1}, & \beta \geq \beta_*. \end{cases}
\end{aligned}
\tag{10}
$$

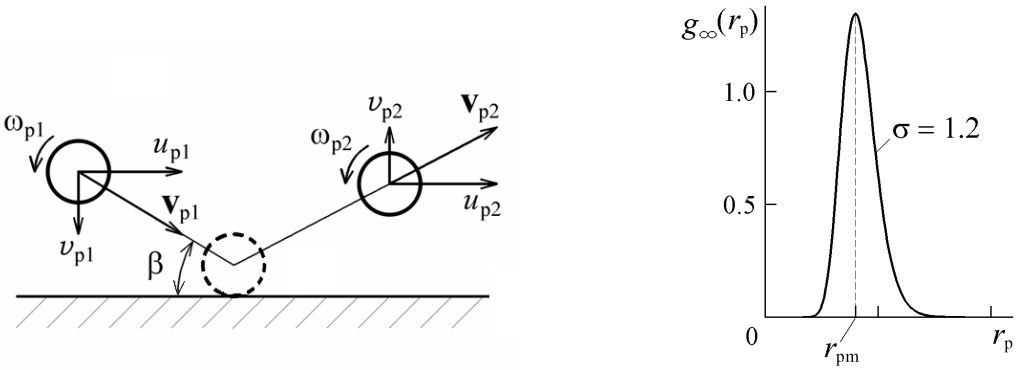

Figure 2: Schematic of a collision (left) and Log-normal law for particles' distribution in size (right).

Here, a_n and a_τ are the restitution coefficients; β_* is the critical value of β: if $\beta < \beta_*$ we have a sliding collision, if $\beta \geq \beta_*$ a collision is non-sliding. The formulae for calculation of the restitution coefficients are taken from [11,12]

$$
\begin{aligned}
a_n &= 1 - \{1 - \exp[-0.1\, V_{\rm p1}^{0.61}]\}\sin\beta, \qquad V_{\rm p1} = (u_{\rm p1}^2 + v_{\rm p1}^2)^{1/2}, \\
a_\tau &= C_0 + C_1\left(\frac{\pi}{2} - \beta\right)^2 + C_2\left(\frac{\pi}{2} - \beta\right)^4 + C_3\left(\frac{\pi}{2} - \beta\right)^6.
\end{aligned}
\tag{11}
$$

The coefficients in the last formula and the critical angle β_* depend on the wall and particle materials. In calculations, they were taken as follows: $C_0 = 0.690$, $C_1 = -0.288$, $C_2 = 0.114$,

$C_3 = 0.0219$ and $\beta_* = 0.1911$. These values correspond to particles from hard materials like corundum or silicon dioxide, and a steel wall.

In the majority of papers on two-phase gas-particle flow, the particles are assumed to be monosized. However, in practice particles are distributed in size that results in mixing of particles of different size in a disturbed flow. In the present study we consider also polydisperse particles. The Log-normal distribution of particles in size in an undisturbed flow is used in calculations. In this case, the particle mass frequency distribution function has the form

$$g_\infty(r_\mathrm{p}) = \frac{1}{\sqrt{2\pi}\, r_\mathrm{p}\, \ln\, \sigma}\, \exp\left[-\left(\frac{\ln\, r_\mathrm{p} - \ln\, r_g}{\sqrt{2}\, \ln\, \sigma}\right)^2\right]. \tag{12}$$

The parameter r_g is related with the most probable particle radius $r_{\mathrm{p}m}$ by $r_g = r_{\mathrm{p}m} \exp(\ln^2 \sigma)$. The plot of function (12) for $\sigma = 1.2$ (this value is taken in calculations) is shown in Fig. 2 (right).

3 NUMERICAL METHOD

3.1 Computational domain and boundary conditions

Computation domain in (xy)-plane consists of two blocks A and B (see Fig. 3). The block A moves together with a rotor blade, and B is stationary. A structured curvilinear grid fitted to the blade contours is introduced in each block. Both grids are refined to the blade surfaces and in the areas behind blades to resolve the flow structure inside the boundary layers and in the wakes. The total length of both blocks in the direction of an undisturbed flow is equal to 4.4 l (l is the airfoil chord).

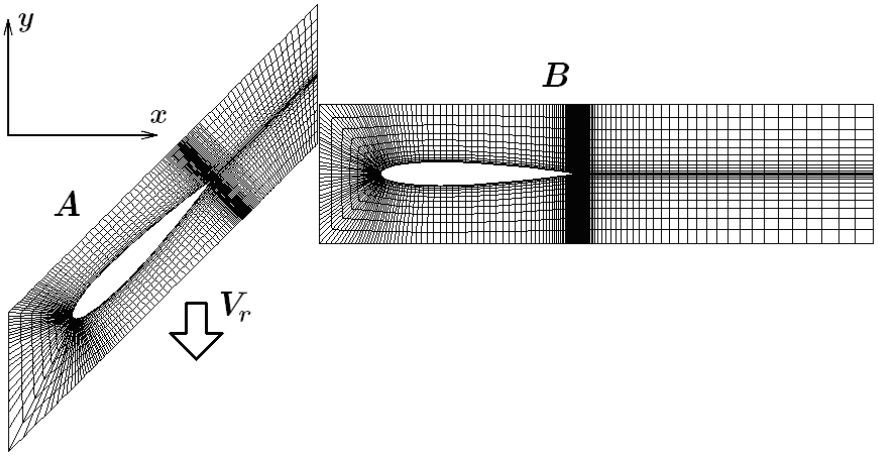

Figure 3: Computational domain and schematic of a grid.

At the airfoil surfaces, the no-slip condition and the constant-temperature wall condition are enforced for the Navier–Stokes equations.

The periodic conditions in y-direction are set at the top and bottom boundaries of each block. This is possible if no large-scale areas of separated flow arise. At the inflow boundary of the moving block the gas velocity and the density are calculated from the given total enthalpy and entropy in the undisturbed flow, and the pressure is extrapolated from the computation domain. At the outflow boundary of the stationary block the pressure is taken equal to $1.2\,p_\infty$ (this value agrees with some experiments) and other parameters are extrapolated from the computation domain. Such a technique is in agreement with the characteristic properties of gas dynamic equations.

A special matching procedure used at the contact boundary between the moving and stationary blocks will be described below in Subsection 3.3.

At the initial instant $t = 0$, a uniform flow with the undisturbed parameters is taken in the whole domain, and then computational simulation of the carrier gas flow is going on up to a quasi-time-periodic solution is reached. After this the particles are introduced into the simulation procedure.

3.2 Finite-volume scheme for the Navier–Stokes equations

An explicit finite-volume method is used for numerical solving the Navier–Stokes equations (1). Consider a cell C_i of the grid (Fig. 4). Integrating the equations (1) over a volume of this cell and applying the Gauss's theorem we obtain these equations in the following integral form:

$$\frac{\partial}{\partial t}\int\limits_{\Omega_i}\mathbf{Q}\,d\Omega+\oint\limits_{S_i}\mathbf{F}dS=\oint\limits_{S_i}\mathbf{G}dS,\quad \mathbf{F}=\mathbf{F}_x n_x+\mathbf{F}_y n_y,\quad \mathbf{G}=\mathbf{G}_x n_x+\mathbf{G}_y n_y. \tag{13}$$

Here Ω_i and S_i are the volume and the surface of the cell C_i, $\mathbf{n}=(n_x,n_y)$ is a unit vector normal to S_i and directed outward. In the plane (xy), Ω_i and S_i are considered as the square and the boundary of a cell.

We represent the integrals over S_i as a sum of integrals over separate cell faces S_{ij} ($j=1,2,3,4$), and apply the mean value theorem to calculate all the integrals in (13). Then we denote flow parameters at instants t and $t+\Delta t$ by superscripts n and $n+1$, respectively, and approximate the derivative $\partial/\partial t$ by a finite-difference. The final discrete approximation of (13) takes the form:

$$\mathbf{Q}_i^{n+1}=\mathbf{Q}_i^n-\frac{\Delta t}{\Omega_i}\sum_{j=1}^{4}\mathbf{F}_{ij}^n S_{ij}+\frac{\Delta t}{\Omega_i}\sum_{j=1}^{4}\mathbf{G}_{ij}^n S_{ij}. \tag{14}$$

Here $\mathbf{Q}^n$ and $\mathbf{Q}^{n+1}$ are ascribed to the center of i-th cell, $\mathbf{F}_{ij}$ and $\mathbf{G}_{ij}$ are the vectors of "inviscid" and "viscous" fluxes of $\mathbf{Q}$ through the j-th face of i-th cell.

At first, we describe briefly the method of calculation of $\mathbf{F}_{ij}$. In the present study, the "inviscid" fluxed are calculated from the Roe scheme [13] with the use of the correction suggested by Harten [14]. Introduce the Jacob's matrix $A=\partial\mathbf{F}/\partial\mathbf{Q}$. Their eigenvalues $\lambda^{(k)}$ are found from the characteristic equation $\det(A-\lambda I)=0$. In our case, the eigenvalues $\lambda^{(1)}$, $\lambda^{(2)}$, $\lambda^{(3)}$,

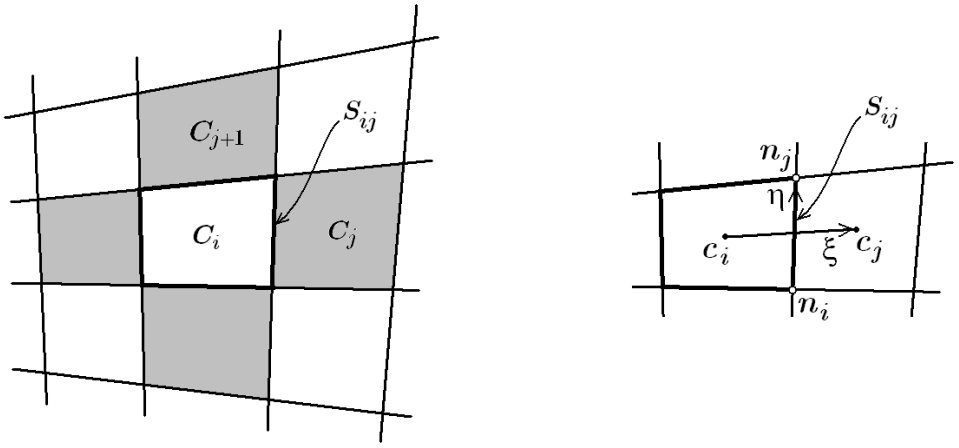

Figure 4: Cell C_i and its environment.

and $\lambda^{(4)}$ are equal to v_n, v_n, $v_n + c$ and $v_n - c$, respectively, where $v_n = u\,n_x + v\,n_y$ is the gas velocity component normal to a cell face, and c is the speed of sound. Denote R and L the matrices with the columns from right and left eigenvectors of the matrix A. These matrices have the form:

$$R = \begin{pmatrix} 1 & 0 & \dfrac{\rho}{2c} & \dfrac{\rho}{2c} \\ u & \rho n_y & \dfrac{\rho}{2c}(u + cn_x) & \dfrac{\rho}{2c}(u - cn_x) \\ v & -\rho n_x & \dfrac{\rho}{2c}(v + cn_y) & \dfrac{\rho}{2c}(v - cn_y) \\ \dfrac{1}{2}(u^2 + v^2) & \rho v_\tau & \dfrac{\rho}{2c}(H + cv_n) & \dfrac{\rho}{2c}(H - cv_n) \end{pmatrix}, \tag{15}$$

$$L = \begin{pmatrix} 1 - \dfrac{\gamma - 1}{2}\mathrm{M}^2 & (\gamma - 1)\dfrac{u}{c^2} & (\gamma - 1)\dfrac{v}{c^2} & -\dfrac{\gamma - 1}{c^2} \\ -\dfrac{v_\tau}{\rho} & \dfrac{n_y}{\rho} & \dfrac{-n_x}{\rho} & 0 \\ \dfrac{c}{\rho}\left(\dfrac{\gamma - 1}{2}\mathrm{M}^2 - \dfrac{v_n}{c}\right) & \dfrac{1}{\rho}\left(n_x - (\gamma - 1)\dfrac{u}{c}\right) & \dfrac{1}{\rho}\left(n_y - (\gamma - 1)\dfrac{v}{c}\right) & \dfrac{\gamma - 1}{\rho c} \\ \dfrac{c}{\rho}\left(\dfrac{\gamma - 1}{2}\mathrm{M}^2 + \dfrac{v_n}{c}\right) & -\dfrac{1}{\rho}\left(n_x + (\gamma - 1)\dfrac{u}{c}\right) & -\dfrac{1}{\rho}\left(n_y + (\gamma - 1)\dfrac{v}{c}\right) & \dfrac{\gamma - 1}{\rho c} \end{pmatrix},$$

where $H = c^2/(\gamma - 1) + (1/2)(u^2 + v^2)$, $v_\tau = u\,n_y - v\,n_x$, and M is the Mach number.

For calculation of the vector $\mathbf{F}_{ij}$ in a summand of the first sum in (14), we consider j-th face of i-th cell. This face is the boundary between i-th cell and an adjacent j-th one. Denote gas parameters in i-th cell at j-th face by subscript l (left), and parameters at the same face in

j-th cell by subscript r (right). This corresponds to path-tracing the boundary of i-th cell in an anti-clockwise direction. The vector $\mathbf{F}_{ij}$ is calculated as follows (subscript i is omitted for short):

$$\mathbf{F}_j = \frac{1}{2}(\mathbf{F}(\mathbf{Q}_r) + \mathbf{F}(\mathbf{Q}_l) - R_j \Lambda_j L_j (\mathbf{Q}_r - \mathbf{Q}_l)), \tag{16}$$

where

$$\Lambda_j = \begin{pmatrix} \psi(\lambda_j^{(1)}) & 0 & 0 & 0 \\ 0 & \psi(\lambda_j^{(2)}) & 0 & 0 \\ 0 & 0 & \psi(\lambda_j^{(3)}) & 0 \\ 0 & 0 & 0 & \psi(\lambda_j^{(4)}) \end{pmatrix}. \tag{17}$$

Recall that $\mathbf{F} = \mathbf{F}_x n_x + \mathbf{F}_y n_y$ (see (13)), and $\mathbf{Q}$, $\mathbf{F}_x$ and $\mathbf{F}_y$ are defined by (2). The components of matrices R_j and L_j, as well as the eigenvalues $\lambda_j^{(k)}$ ($k = 1, 2, 3, 4$), are calculated using the values of gas parameters determined by the following relations:

$$\rho_j = \sqrt{\rho_l}\sqrt{\rho_r}, \qquad u_j = \frac{u_l\sqrt{\rho_l} + u_r\sqrt{\rho_r}}{\sqrt{\rho_l} + \sqrt{\rho_r}}, \qquad v_j = \frac{v_l\sqrt{\rho_l} + v_r\sqrt{\rho_r}}{\sqrt{\rho_l} + \sqrt{\rho_r}}, \tag{18}$$

$$H_j = \frac{H_l\sqrt{\rho_l} + H_r\sqrt{\rho_r}}{\sqrt{\rho_l} + \sqrt{\rho_r}}, \qquad c_j = \sqrt{(H_j - (u_j^2 + v_j^2)/2)(\gamma - 1)}.$$

The function $\psi(\lambda)$ is defined by relations [14]

$$\psi(\lambda) = \begin{cases} |\lambda|, & |\lambda| \geq \epsilon, \\ (\lambda^2 + \epsilon^2)/2\epsilon, & |\lambda| < \epsilon, \end{cases} \tag{19}$$

where ϵ is a small positive parameter (in calculations it is taken equal to 0.1). The last relation in (19) is applied to correct an eigenvalue λ in the case when $|\lambda|$ is small enough that can result in oscillations of numerical solution.

For calculation of the components of the vector $\mathbf{Q}$ at j-th face of a i-th cell, a bilinear reconstruction of gas parameters ρ, u, v, p is used. Let ϕ be any of parameters listed above. Its value in the center (x_{Ci}, y_{Ci}) of the cell C_i we denote ϕ_{Ci}, and its dependence on coordinates x and y within the cell we take in the form:

$$\phi(x, y) = \phi_{Ci} + a_i\,(x - x_{Ci}) + b_i\,(y - y_{Ci}). \tag{20}$$

The coefficients a_i and b_i represent the components of the vector $\nabla\phi$, and they are determined with taking account of values of ϕ in all neighbouring cells which have common boundaries with C_i (these cells are shown in Fig. 4 (left) by grey colour). At first, consider two such consecutive cells C_j and C_{j+1}, and build up a bilinear reconstruction for ϕ using the values of ϕ in the centers of three cells: C_i, C_j and C_{j+1}. This procedure gives us a pair of coefficients which we denote $a_i^{(j)}$, $b_i^{(j)}$. Then we repeat the procedure for all combinations of the cell C_i

with other pairs of cells consecutively adjacent to C_i, and find four pairs $a_i^{(j)}$, $b_i^{(j)}$ (j = 1, 2, 3, 4). The final values of a_i and b_i in (20) are calculated as weighting averages with the use of technique which is similar to the WENO reconstruction (see, e.g., [15]):

$$a_i = \frac{\sum\limits_{j=1}^{4} w_j a_i^{(j)}}{\sum\limits_{j=1}^{4} w_j}, \qquad b_i = \frac{\sum\limits_{j=1}^{4} w_j b_i^{(j)}}{\sum\limits_{j=1}^{4} w_j}, \qquad w_j = \frac{1}{\varepsilon + \zeta_j^{\theta}}, \qquad \zeta_j = \left[(a_i^{(j)})^2 + (b_i^{(j)})^2 \right]^{1/2}. \tag{21}$$

Here ε is a small parameter (in calculations, it is taken equal to 10^{-5}). The power θ in the present work is taken as $\theta = 2$. We have to note that the technique of weighting averaging (21) in computational simulation of flow considered in the present paper is much better than the use of "minmod" limiter [14] which also has been applied at the initial stage of the study.

After the coefficients a_i and b_i are found, we calculate the gas parameters at the center of j-th face of the cell C_i using the bilinear reconstruction (20). Then we calculate the components of the vector $\mathbf{Q}$ which is treated as $\mathbf{Q}_l$. Quite similar, the components of the vector $\mathbf{Q}_r$ (enters into (16)) at the same j-th face are calculated.

Consider now the algorithm of calculation of "viscous" flux $\mathbf{G}_{ij}$ through the face S_{ij} in (14). The vector $\mathbf{G}$ is defined by (13), and the vectors $\mathbf{G}_x$ and $\mathbf{G}_y$ entering into (13) have the components defined by (2) with the expressions (3)–(4) for τ_{xx}, τ_{yy}, τ_{xy}, q_x, and q_y. The viscosity μ, and the thermal conductivity k in these expressions depend on the temperature (see relations (4)). To determine the vector $\mathbf{G}_{ij}$ we have to know at the face S_{ij} the following parameters: u, v, T, $\partial u/\partial x$, $\partial v/\partial x$, $\partial u/\partial y$, $\partial v/\partial y$, $\partial T/\partial x$ and $\partial T/\partial y$. For subsequent reasoning and mathematical transformations, we denote any of the listed parameters by f. In the present study, u, v and T at the face S_{ij} are calculated as the average of these parameters at the centers c_i and c_j of i-th and j-th cells (Fig 4, right): $f = (1/2)(f_{c_i} + f_{c_j})$. To calculate the derivatives $\partial f/\partial x$ and $\partial f/\partial y$ at the face S_{ij}, we first introduce the local coordinates (ξ, η) (see Fig. 4) and calculate the derivatives $\partial f/\partial \xi$ and $\partial f/\partial \eta$ from the approximate formulae:

$$\frac{\partial f}{\partial \xi} = \frac{f_{c_j} - f_{c_i}}{\Delta \xi}, \qquad \frac{\partial f}{\partial \eta} = \frac{f_{n_j} - f_{n_i}}{\Delta \eta}, \tag{22}$$

where f_{c_i}, f_{c_j} are the values of f at the centers c_i, c_j of i-th and j-th cells, $\Delta\xi$ and $\Delta\eta$ are the distance between the centers of these cells, and between the grid nodes n_i and n_j, respectively. Any gas parameter (f) at a grid node is calculated as the average of its values at the centers of all cells surrounding the node. Then we calculate the derivatives $\partial f/\partial x$ and $\partial f/\partial y$ from the following relations:

$$\frac{\partial f}{\partial x} = \frac{\partial f}{\partial \xi}\frac{\partial \xi}{\partial x} + \frac{\partial f}{\partial \eta}\frac{\partial \eta}{\partial x}, \qquad \frac{\partial f}{\partial y} = \frac{\partial f}{\partial \xi}\frac{\partial \xi}{\partial y} + \frac{\partial f}{\partial \eta}\frac{\partial \eta}{\partial y}, \tag{23}$$

where

$$\frac{\partial \xi}{\partial x} = \frac{\partial y}{\partial \eta} J^{-1}, \qquad \frac{\partial \xi}{\partial y} = -\frac{\partial x}{\partial \eta} J^{-1}, \qquad \frac{\partial \eta}{\partial x} = -\frac{\partial y}{\partial \xi} J^{-1}, \qquad \frac{\partial \eta}{\partial y} = \frac{\partial x}{\partial \xi} J^{-1}, \tag{24}$$

$$J = \frac{\partial x}{\partial \xi}\frac{\partial y}{\partial \eta} - \frac{\partial x}{\partial \eta}\frac{\partial y}{\partial \xi}.$$

After we calculate the derivatives $\partial u/\partial x$, $\partial v/\partial x$, $\partial u/\partial y$, $\partial v/\partial y$, $\partial T/\partial x$ and $\partial T/\partial y$, we substitute them together with u, v and T into relations (2)–(4) and find the components of $\mathbf{G}_x$ and $\mathbf{G}_y$. Then we determine $\mathbf{G}_{ij}$. This algorithm is applied to all faces S_{ij} (j = 1, 2, 3, 4) of the cell C_i.

The time step Δt in (14) is chosen from the conventional stability condition.

3.3 Matching procedure at the boundary of the moving and stationary blocks

For the "rotor" and "stator" blocks we use two different system of coordinates, every of each is immovable relatively to the corresponding block. In calculations of cells adjacent to the boundary between the moving (A) and stationary (B) blocks (see Figs. 3 and 5), we use a moving coordinate system for boundary cells in block A and an immovable one for cells in block B. It is necessary in this case to recalculate the y-component of the gas velocity. After it we apply the finite-volume scheme to near-boundary cells. The main problem is to find "inviscid" and "viscous" fluxes through the common boundary of adjacent cells of different blocks.

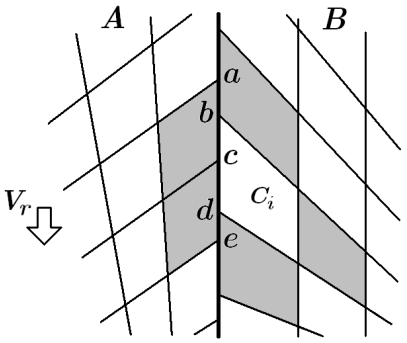

Figure 5: Boundary between the moving (A) and stationary (B) blocks and a near-boundary cell C_i.

Consider, for example, the near-boundary cell C_i and the surrounding cells shown by grey colour in Fig. 5. The "inviscid" flux $\mathbf{F}$ through the face bd can be calculated in the manner quite similar to that described above for a inner cell. However in our example, we have to determine the coefficients in the bilinear reconstruction (20) using not four, but five groups of cells. Every group includes the cell C_i and two consecutive "grey" ones. As a result, we find five pairs $a_i^{(k)}$ and $b_i^{(k)}$ (k = 1, ... , 5). Then we apply the procedure of weighing averaging (21) to $a_i^{(k)}$ and $b_i^{(k)}$ and find a_i and b_i. After it we can calculate gas parameters in C_i at any point of the face bd from (20). We calculate them at the centers of bc and cd, and use these values to determine the vector $\mathbf{Q}$ which is treated as $\mathbf{Q}_l$ in subsequent calculations. Similar to this we calculate $\mathbf{Q}_r$ at the centers of bc and cd of the corresponding "grey" cells. Now we can calculate the flux $\mathbf{F}$ through bc and cd from (16). The flux through the whole face bd of the cell C_i is equal to the sum of fluxes through bc and cd.

"Viscous" fluxes through the parts bc and cd is calculated with the use of the relations (22)–(24), and the total flux through the face bd of the cell C_i is equal to their sum.

3.4 Calculation of particles' motion

After a quasi-time-periodic solution of the Navier–Stokes equations for the carrier gas is reached, particles are introduced into the simulation procedure, and the motion of particles is calculated simultaneously with ongoing solving the equations for the carrier gas. Initially, particles are placed in a cloud of finite width h (see Fig. 1), the position of each particle within a cloud is random, and it is chosen from the equiprobable distribution. All particles have the same velocity $\mathbf{V}_\infty$. The joint gas–particle flow calculation over a time step Δt consists of two stages. At first, the Navier–Stokes equations are solved from t^n to $t^{n+1} = t^n + \Delta t$ as it is described above, and then the equations (5) for every particle are solved by the modified Euler method. Write the equations (5) in the compact form

$$\frac{d\mathbf{X}}{dt} = \mathbf{U}(\mathbf{X}), \quad \text{where} \quad \mathbf{X} = \begin{pmatrix} m_\mathrm{p} u_\mathrm{p} \\ m_\mathrm{p} v_\mathrm{p} \\ J_\mathrm{p} \omega_\mathrm{p} \\ x_\mathrm{p} \\ y_\mathrm{p} \end{pmatrix}, \quad \mathbf{U}(\mathbf{X}) = \begin{pmatrix} f_{\mathrm{D}x} + f_{\mathrm{M}x} \\ f_{\mathrm{D}y} + f_{\mathrm{M}y} \\ l_\mathrm{p} \\ u_\mathrm{p} \\ v_\mathrm{p} \end{pmatrix}. \tag{25}$$

The particle drag force $\mathbf{f}_\mathrm{D}$, the lift Magnus force $\mathbf{f}_\mathrm{M}$, and the torque l_p (in a 2D-flow the torque $\mathbf{l}_\mathrm{p}$ has only one non-zero component which is normal to the plane (x, y), it is denoted by l_p) are determined by relations (6)–(9).

Numerical integration of the equation (25) with respect to time from t^n to $t^{n+1} = t^n + \Delta t$ is carried out as follows:

$$\mathbf{X}^* = \mathbf{X}^n + \Delta t\, \mathbf{U}(\mathbf{X}^n), \qquad \mathbf{X}^{n+1} = \mathbf{X}^n + \Delta t(\mathbf{U}(\mathbf{X}^n) + \mathbf{U}(\mathbf{X}^*))/2. \tag{26}$$

This is a predictor-corrector method of the second order.

The total number of particles in a cloud is varied from 50,000 to 5,000,000.

4 RESULTS OF COMPUTATIONAL SIMULATION AND DISCUSSION

4.1 Input data

Parameters of the cascades and flow properties are taken in calculations close to those which are typical for an inlet compressor of a turbojet engine. The chord of airfoils is equal to $l = 10$ cm, the cascade step $s = 7$ cm, the angle of attack $\beta = 45°$, the profile of blades is NACA0012, the main (undisturbed) flow velocity $V_\infty = 200$ m/s, the cascade velocity $V_r = 150$ m/s, the carrier gas is air ($\Re = 287$ J/(kg K), $c_p/c_V = 1.4$; coefficients in the Sutherlend formula (4): $\mu_0 = 1.71 \cdot 10^{-5}$ N·s/m^2, $T_0 = 288$ K, $S_0 = 117$ K), the Prandtl number Pr = 0.72, the flow density and temperature ρ_∞ = 1.21 kg/m^3 and $T_\infty = 288$ K. These values correspond to the Mach number M_∞ = 0.59. The particle and blade materials are silicon dioxide and steel, respectively.

4.2 Results for the carrier gas

In parallel with numerical solving the Navier–Stokes equations we also solved the Euler equations using the same grids and the same finite volume method but with "viscous" terms equal to zero. The main aim here was to understand the role of viscous effects in forming the flow structure and also to estimate "a numerical scheme viscosity". Comparison of instant fields of different gas properties are shown in Figs. 6, 7 and 8. As is clearly seen from Fig. 6, (a), in the case of the Euler equations we have nearly homogeneous entropy field that is, on the one hand, in good agreement with the theoretical statement that the entropy in a flow of ideal gas remains constant, and on the other hand, testifies that the numerical method has rather low "scheme viscosity". In the field of a viscous gas (Fig. 6, (b)) we see spots with much higher entropy than in the main stream. These inhomogeneities arise due to the entropy production in boundary layers at the blade surfaces and inside separated eddies in the vortex wakes behind blades. Eddies generate pressure waves in the flow field (Fig. 7, (a)). These waves are absent in the solution of the Euler equations (Fig.7, (b)). Fields of the Mach number in both cases (Fig. 8) correspond in structure to those for the entropy function (Fig. 6). As is seen, flow is subsonic everywhere in the reference system connected with the "stator" cascade. In the outflow boundary of the calculation domain (right boundary of the stationary grid block), the gas velocity, the density, and the temperature reach nearly constant values: V = 115 m/s, $\rho = 1.56$ kg/m^3, $T = 304$ K. These parameters correspond to the Mach number $M = 0.33$.

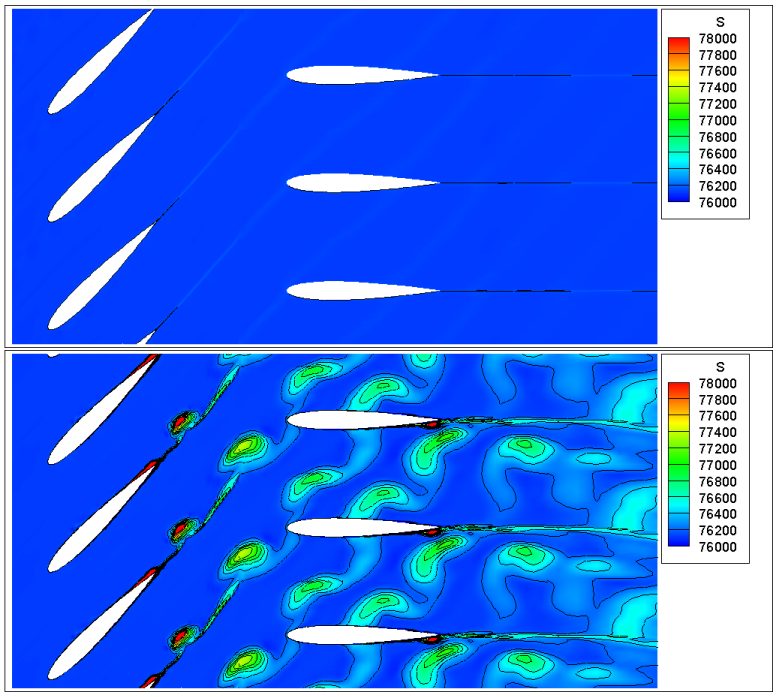

Figure 6: Instant field of the entropy function $\vartheta = p/\rho^\gamma$: (a) Euler equations; (b) Navier–Stokes equations.

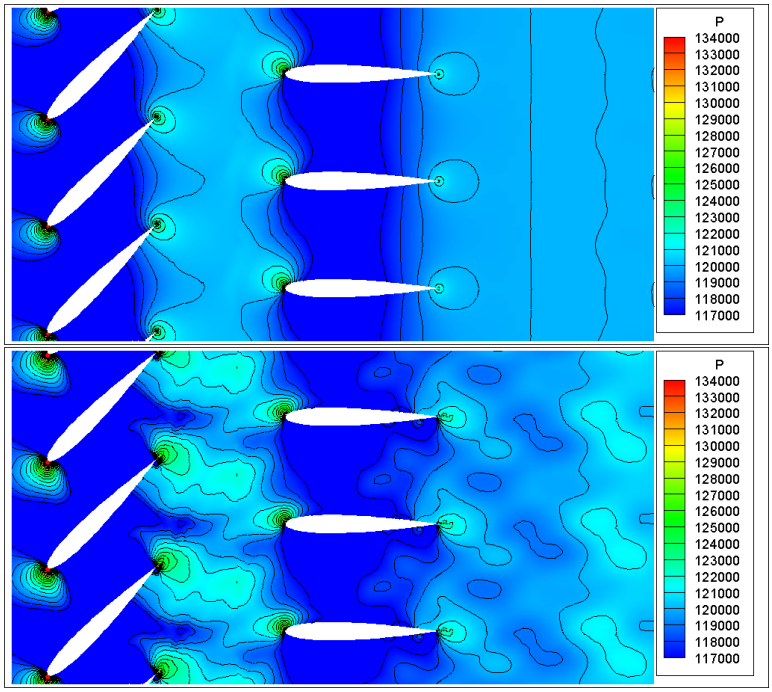

Figure 7: Instant field of the pressure: (*a*) Euler equations; (*b*) Navier–Stokes equations.

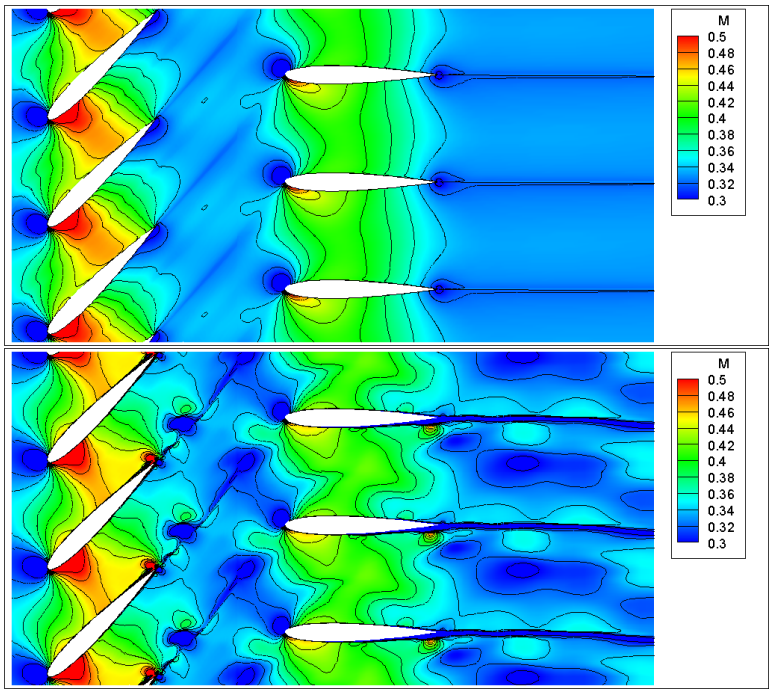

Figure 8: Instant field of the Mach number: (*a*) Euler equations; (*b*) Navier–Stokes equations.

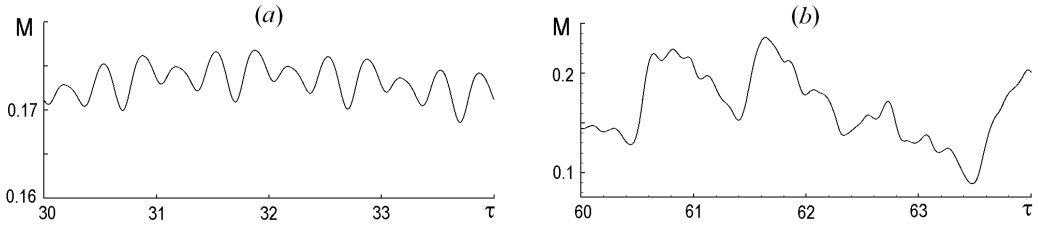

Figure 9: Mach number in front of a stator airfoil as a function of time: (a) Euler equations; (b) Navier–Stokes equations

Computational experiments have shown that numerical solution of the Euler equations reaches with time a strictly periodic behaviour that is illustrated by Fig. 9, (a). In the figure $\tau = t/t_s$, where $t_s = s/V_r$ ($t_s = 0.47 \cdot 10^{-3}$ s for the given values of s and V_r). The period includes three maximums and three minimums. For the Navier-Stokes equations, the time-dependent character of a solution is illustrated by Fig. 9, (b). It is seen that in this case a time-periodic solution is absent. Such a situation is connected with two independent periodic in time processes: separation of eddies from blades, and motion of spatially periodic rotor blades relative to the stator blades with the same spatial period. The first process is determined by the Reynolds number of flow around a blade, whereas the second one is determined by the velocity V_r and the cascade step s. If the periods of both processes are not multiple, their interaction can result in "stochastic" behaviour of flow parameters with time.

4.3 Results for the particle-phase

For visualization of the particle-phase flow we consider a particle cloud of finite width h equal to the airfoil chord l (see Fig. 1). Particles in the cloud were distributed in space randomly by the uniform distribution. All the results given below in this Subsection refer to the carrier gas flow field computed from the Navier–Stokes equations. Instant particle flow patterns at the same moment for different values of the particle radius (in the case of monosized particles) and the most probable particle radius (in the case of Log-normally distributed particles in an undisturbed flow) are shown in Figs. 10–12. Particle radiuses $r_{\rm p} = 5$ μm, 10 μm and 20 μm correspond to the Stokes numbers Stk = 1.70, 6.82 and 27.28, respectively. The Stokes number is defined as the ratio of the particle dynamic relaxation length (with the use of the Stokes law for a particle drag force) to the characteristic length in the flow l: $\mathrm{Stk} = 2\rho_{\rm p} r_{\rm p}^2 V_\infty/(9\mu_\infty l)$.

In all figures, particles not collided with blades, collided only with "rotor" blades, collided only with "stator" blades, and with both "rotor" and "stator" blades are marked by blue, green, red and black colour, respectively.

An initially uniform particle cloud is distorted strongly in the flow, and the distribution of particles in space becomes substantially non-uniform. A redistribution of particles occurs by the action of non-uniform flow field of the carrier gas and by their collisions with blades. For small particles ($Stk < 10$) the effect of boundary layers and vortex wakes is of great importance in the process of redistribution, whereas for large particles ($Stk > 20$) this effect is negligible,

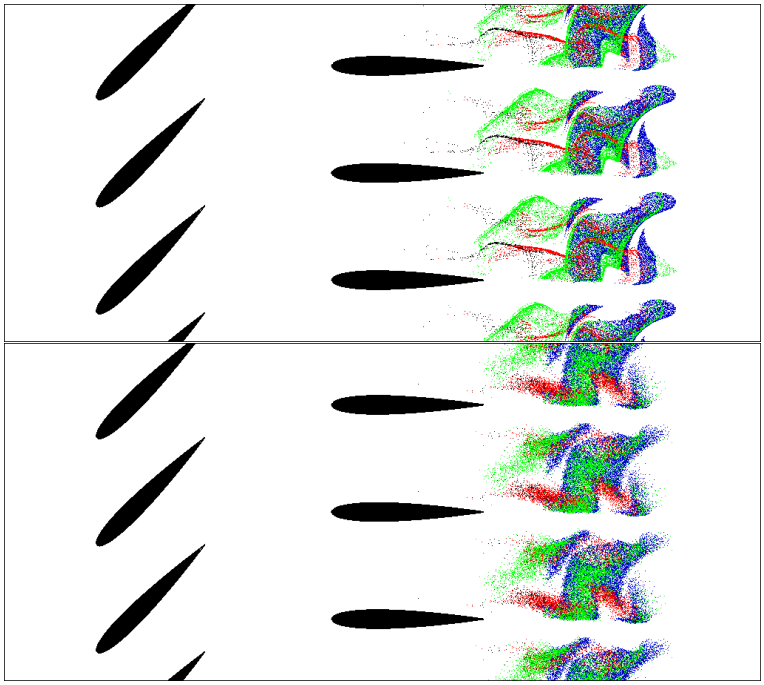

Figure 10: Instant patterns of (a) monosized and (b) polydisperse particles: $r_{\rm p} = r_{\rm pm} = 5$ μm.

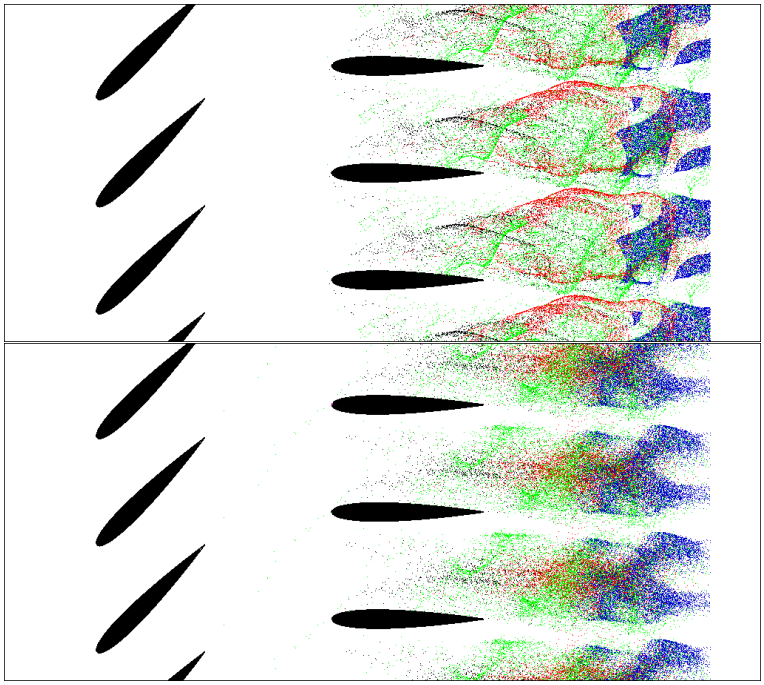

Figure 11: Instant patterns of (a) monosized and (b) polydisperse particles: $r_{\rm p} = r_{\rm pm} = 10$ μm.

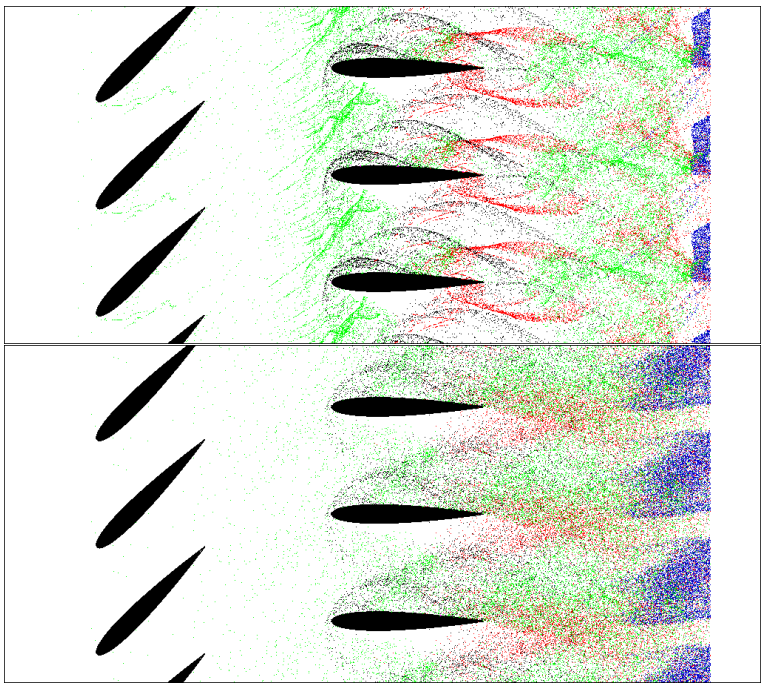

Figure 12: Instant patterns of (a) monosized and (b) polydisperse particles: $r_{\rm p} = r_{\rm pm} = 20$ μm.

but the particle-blade collisions play a key role.

The particle distribution in size results in "smearing" the particle concentration field. The physical reason of this effect is mixing of particles of different sizes in a flow.

5 CONCLUSION

The present investigation of dusty gas flow through a set "rotor–stator" of 2D-cascades has shown that dispersed particles are redistributed strongly in the flow. The behaviour of the particle phase depends substantially on the particle size. Motion of small particles is governed mainly by the carrier gas flow which is rather complicated due to separation of eddies from blades with forming the vortex wakes. Large particles colliding with the blades rebound from them and the rebounded particles can collide later with both, nearest and far blades, that makes the particle phase flow more complicated. In the case of monosized particles, the narrow layers with high particle concentration arise. Mixing of particles of different sizes results in smearing of these layers. This allow us to conclude that in actual dusty gas flows the erosive damage from the particles' impacts is less that it can be predicted by the classical two-phase flow theory.

ACKNOWLEDGEMENTS

The authors wish to express their thanks to Dr. Sergei Panfilov for helpful discussions of this work in different stages. This study was supported by the Russian Foundation for Basic Research under grant No. 09-08-00888.

APPENDIX

We would like to pay attention to one problem which in the commonly accepted theory is thought to be solved and closed. The case in point is the mechanism of flow separation from the body with a smooth contour and following development of a vortex wake. Such a phenomenon is a subject of the boundary layer theory (see, e.g., the well-known monograph "Boundary Layer Theory" by H. Shlihting) which explains the separation by modification of a velocity profile in a viscous boundary layer at the body surface. However, our calculations clearly show that separation from a smooth body can be not connected with the boundary layer effects. Three instant flow patterns past a circular cylinder are given below in Fig. 13. All they are obtained by computational simulation with the use of the same very fine grid. The first pattern is obtained by numerical solving the Euler (*inviscid*) equations. The second one refers to the Navier–Stokes equations but *without non-sleep conditions* at the cylinder surface. The last pattern corresponds to the Navier–Stokes equations and *traditional non-sleep conditions*. As is seen, all these patterns are in close agreement. In all cases we observe the flow separation and the development of the vortex street. The Strukhal number in all cases is practically the same. In our opinion, this result is an evidence of that in some situations the flow separation and the structure of the vortex wake can be calculated without taking the boundary layer effects into account.

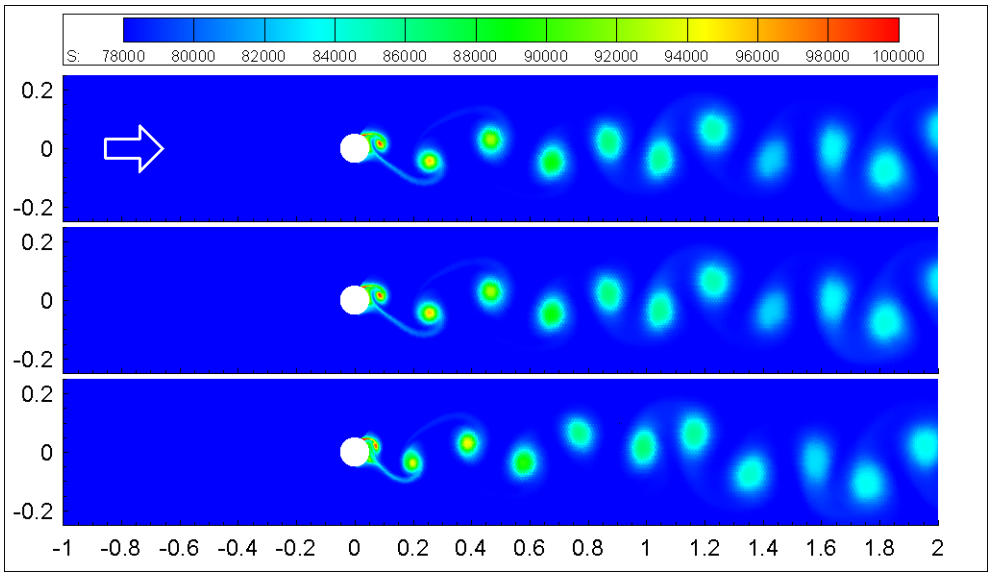

Figure 13: Structures of the vortex wake behind a cylinder calculated by using three different flow models.

REFERENCES

[1] W. Tabakoff and A. Hamed, Aerodynamic effect on erosion in turbomachinery, *Proc. JSME and ASME 1977 Joint Gas Turbine Congress*. Tokyo, Japan, 574–581 (1977).

[2] G. Yu. Stepanov, Hydrodynamics of cascades of turbomachines, *FIZMATLIT*, Moscow (1962). [in Russian]

[3] M. F. Hussein and W. Tabakoff, Calculation of particle trajectories in a stationary two-dimensional cascade, *Dept. of Aero. Engng.* TR 72-27, University of Cincinnati, AD-764267 (1972).

[4] M. F. Hussein and W. Tabakoff, Dynamic behavior of solid particles suspended by polluted flow in a turbine cascade, *J. Aircraft*, **10**, (7), 434–440 (1973).

[5] Yu. M. Tsirkunov, Gas-particle flows around bodies – key problems, modeling and numerical analysis, *Proc. Fourth International Conference on Multiphase Flow*, ICMF'2001, E. Michaelides Ed., New Orleans, LA, USA, Paper n°607 (2001).

[6] D. A. Anderson, J. C. Tannehill and R. H. Pletcher, Computational Fluid Mechanics and Heat Transfer, *Hemisphere Publ. Corp.*, New York (1984).

[7] Ch. B. Henderson, Drag coefficient of spheres in continuum and rarefied flows, *AIAA J.*, **14**, 707–708 (1976).

[8] S. I. Rubinow and J. B. Keller, The transverse force on a spinning sphere moving in a viscous fluid, *J. Fluid Mech.*, **11**, 447–459 (1961).

[9] B. Oesterlé and T. Bui Dinh, Experiments on the lift of a spinning sphere in a range of intermediate Reynolds numbers, *Experim. in Fluids*, **25**, 16–22 (1998).

[10] S. R. C. Dennis, S. N. Singh and D. B. Ingham, The steady flow due to a rotating sphere at low and moderate Reynolds numbers, *J. Fluid Mech.*, **101**, 257–279 (1980).

[11] Yu. M. Tsirkunov, S. V. Panfilov and M. B. Klychnikov, Semiempirical model of impact interaction of a disperse impurity particle with a surface in a gas suspension flow, *J. Engng. Physics and Thermophysics*, **67** (5-6), 1018–1025 (1994).

[12] V.A. Lashkov, Experimental determination of the coefficients of restitution of particles in the flow of a gas suspension in a collision against the surface, *J. Engineering Physics*, **60**, (2), 154–159 (1991).

[13] P.L. Roe, Approximate Riemann solvers, parameter vector and difference schemes, *J. Comput. Phys.*, **43**, (2), 357–372 (1981).

[14] H.C. Yee and A. Harten, Implicit TVD schemes for hyperbolic conservation laws in curvilinear coordinates, *AIAA J.*, **25**, (2), 266–274 (1987).

[15] W.R. Wolf and J.L.F. Azevedo, Compressible aerodynamic flow simulation using ENO and WENO schemes in a finite volume unstructured grid context, *Tend. Mat. Apl. Comput.*, **6**, (2), 325–335 (2005).